Journal Name

ARTICLE TYPE

Cite this: DOI: 10.1039/xxxxxxxxxx

Macroscopic and Tunable Nanoparticle Superlattices †

Honghu Zhang,[a] Wenjie Wang,[b] Surya Mallapragada,[c] Alex Travesset,[d] and David Vaknin*[d]

Received Date
Accepted Date

DOI: 10.1039/xxxxxxxxxx

www.rsc.org/journalname

We describe a robust method to assemble nanoparticles into highly ordered superlattices by inducing aqueous phase separation of neutral capping polymers. Here we demonstrate the approach with thiolated polyethylene-glycol-functionalized gold nanoparticles (PEG-AuNPs) in the presence of salts (for example, K_2CO_3) in solutions that spontaneously migrate to the liquid-vapor interface to form a Gibbs monolayer. We show that by increasing salt concentration, PEG-AuNP monolayers transform from two-dimensional (2D) gas-like to liquid-like phase and eventually, beyond a threshold concentration, to a highly ordered hexagonal structure, as characterized by surface sensitive synchrotron X-ray reflectivity and grazing incidence X-ray diffraction. Furthermore, the method allows control of the inplane packing in the crystalline phase by varying the K_2CO_3 and PEG-AuNPs concentrations and the length of PEG. Using polymer-brush theory, we argue that the assembly and crystallization is driven by the need to reduce surface tension between PEG and the salt solution. Our approach of taking advantage of the phase separation of PEG in salt solutions is general (i.e., can be used with any nanoparticles) leads to high-quality macroscopic and tunable crystals. Finally, we discuss how the method can also be applied to the design of orderly 3D structures.

1 Introduction

Self-assembly of nanoparticles and molecular-scale building blocks into hierarchically designed ordered structures provides a promising route for the production of metamaterials and nanodevices through bottom-up approaches.[1–6] Particularly, chemically stable gold nanoparticles (AuNPs) that seem to possess desirable optical and electronic properties have been assembled into three dimensional (3D) ordered structures by use of complementary single-stranded DNA or DNA origami with unique programmable features.[4–8] Concomitantly, two-dimensional (2D) self-assembly of AuNPs at solid- or vapor-liquid interfaces have also been developed,[9–11] providing valuable understanding of general mechanisms involved in self-assembly that can be readily applied in other dimensions. Employing a self- and guided-assembly approach, it has been shown that capped AuNPs, AgNPs, or magnetite with various surfactants (including thiolated-acyl chains, -PEG, and others) can be manipulated in a Langmuir trough to form ordered 2D domains, which can be transferred to solid support by the Langmuir-Blodgett technique for further applications[12–21]. Recently, it has been shown that unpaired thiolated ssDNA functionalized AuNPs (ssDNA-AuNPs) self-assemble and crystallize at gas-solution interfaces spontaneously simply by tuning various salts concentrations.[22–24] These studies established that the complexed ssDNA-AuNP is amphiphilic in character by virtue of the polyelectrolytic nature of DNA that competes with the hydrophobicity that is inadervertently introduced in the thiolating process of DNA.[24] Another approach to 2D assembly exploits electrostatic interactions between a positively charged template formed by a Langmuir monolayer with desired charged headgroups lipids and the negatively charged ssDNA-AuNPs or even unfunctionalized (bare) AuNPs.[25–27] These studies point to the possibility that the functionalizing DNA can be replaced by macromolecules that display intrinsic amphiphilic character. Thus, inspired by our findings,[24] we have embarked on a robust approach to explore the interfacial and 3D self-assembly of gold nanoparticles by functionalizing them with polyelectrolytes and amphiphilic polymers. Here, we report on the properties and self-assembly of polyethylene-glycol (PEG)-functionalized AuNPs (PEG-AuNPs). PEG is a remarkable linear polymer that resides on the hydrophobic/hydrophilic edge where one or the other (hydrophobic or hydrophilic) can be readily tweaked by varying salts

[a] Ames Laboratory and Department of Materials Science and Engineering, Iowa State University, Ames, Iowa 50011, USA.
[b] Division of Materials Sciences and Engineering, Ames Laboratory, U.S. DOE, Ames, Iowa 50011, USA.
[c] Ames Laboratory and Department of Chemical and Biological Engineering, Iowa State University, Ames, Iowa 50011, USA.
[d] Ames Laboratory and Department of Physics and Astronomy, Iowa State University, Ames, Iowa 50011, USA. Tel: (515) 294-6023; E-mail: vaknin@ameslab

† Electronic Supplementary Information (ESI) available. See DOI: 10.1039/b000000x/

concentrations, pH, and temperature.[28,29] These properties of PEG mixed with dextran or salts have been widely used in the separation and extraction of macromolecules and organelles of cells by the so called aqueous biphasic systems technique (ABS).[30–32] Owing to PEG's biocompatibility and the low cytotoxicity of Au, studies of PEG-AuNPs have been focused towards nanomedicine applications.[33–35] Grazing incidence small-angle X-ray scattering (GISAXS) and X-ray reflectivity (XRR) are used to determine the in-plane structure and surface-normal density profile, respectively, of self-assembled PEG-AuNPs at the vapor-liquid interface by manipulating the concentration of a specific salt, K_2CO_3 that has been efficiently used in ABS.[30,31] The evolution of 2D PEG-AuNP superlattice formation is systematically studied with two kinds of PEG (molecular weight of 6000 and 800) by manipulating K_2CO_3 and PEG-AuNP concentrations.

2 Experimental

2.1 Reagents and Materials

Poly(ethylene glycol) methyl ether thiol (PEG-SH; Sigma-Aldrich) with average molecular weight of 800 and 6000 g/mol (the number of monomer $N_r = 18$ and 136, respectively; Kuhn length $b = 7.24$ Å; See the Supplementary Information) was dissolved in degassed Millipore water with slight sonication. The freshly-prepared PEG-SH solution was added to aqueous suspension of citrate-stabilized gold nanoparticles (AuNPs, with nominal size of 10 nm; Ted Pella) in large excess (molar ratio of PEG-SH/AuNP $\approx$ 6000) under vigorous stirring. The mixture of PEG-SH and AuNPs was gently stirred at room temperature for one day to allow for maximum PEG loading after ligand exchange. The as-prepared PEG-AuNPs were concentrated via centrifugation (at $20000g \times$ 1h). The supernatant was discarded and the precipitate was collected and redispersed in Millipore water. This washing process with centrifugation and redispersion was done at least twice prior to further measurements. The concentration of PEG-AuNPs was determined by UV-Visible absorption measurements. Aqueous solution of potassium carbonate (anhydrous, K_2CO_3; Fisher Scientific) was prepared and mixed with PEG-AuNPs suspensions at desired concentrations of K_2CO_3 (0.05–1000 mM) and PEG-AuNPs (0.05–10 nM) prior to X-ray measurements. We note that PEG-AuNPs form visible precipitates at 1 M K_2CO_3 after overnight incubation, while they are stable as suspension for months at low K_2CO_3 concentrations.

2.2 Experimental Setup

Specular X-ray reflectivity (XRR) and grazing incidence small-angle X-ray scattering (GISAXS) measurements were conducted on the liquid surface spectrometer (LSS) at beamline 9ID-B, Advanced Photon Source (APS), Argonne National Laboratory. The aqueous solution of the PEG-AuNPs in absence and presence of K_2CO_3 was contained in a shallow trough (surface area 6×6 cm^2 and enclosed in gas tight canister) where the aqueous surface was illuminated with a highly collimated and monochromatic X-ray beam (photon energy $E = 8.0$ keV and wavelength $\lambda = 1.5497$ Å). For an XRR measurement, a point detector (Bicron) that moves within the scattering plane, was used to collect the X-ray reflection from the surface at the exit angle (with respect to the surface) α_f in such way that $\alpha_f = \alpha_i$, α_i being the X-ray incident angle with respect to the surface. The reflectivity, R, was measured as a function of Q_z that equals $(4\pi/\lambda)\sin\alpha_i$ and is the z-component (along the surface normal) of the moment transfer $\mathbf{Q}$. The trough was allowed to move laterally to provide fresh portions of the surface in the course of the reflectivity measurement. For a GISAXS measurement, a digital, two-dimensional Pilatus 100K detector (487 $\times$ 195 pixels, 172 $\times$ 172 μm per pixel) was placed downstream from the sample and was calibrated with the standard calibrating material, i.e., silver behenate powder. The GISAXS intensity was obtained as a function of the three orthogonal components denoted as (Q_x, Q_y, Q_z), where Q_z component is along the surface normal, while Q_x and Q_y components are parallel to the surface. In this study, Q_y is defined as parallel to the detector surface while $Q_x \approx 0$. Thus, the magnitude of the in-plane scattering vector, Q_{xy}, defined as $\sqrt{Q_x^2 + Q_y^2}$, is practically equivalent to Q_y. In the small angle regime, $Q_y \approx (4\pi/\lambda)\theta$, 2θ being the in-plane scattering angle. The X-ray exposure time and incident beam attenuation were carefully chosen in such way that each GISAXS frame has a good signal to noise ratio and sample radiation damage was minimized. The trough was sealed in a canister that has Kapton windows for X-ray passage. It was purged with water-saturated helium in the course of the X-ray measurements to minimize the background scattering and radiation damage. The instrumental details can be found elsewhere.[36] Solution small-angle X-ray scattering (SAXS) experiments for determining the size of the nanoparticles in suspension were performed on beamline 12ID-B at APS with similar setups employed for biomolecules before.[27,37]

3 Results and Discussion

GISAXS patterns as functions of Q_{xy} and Q_z for aqueous solutions of PEG_{6k}-AuNPs without salts and with 500 mM K_2CO_3 are shown in Fig. 1a. In the absence of salts, sector-shaped and broad circular features at low and high Q_{xy} ranges originate from the form factor of PEG_{6k}-AuNPs, which is dominated by the bare form factor of AuNPs (see SI).[24,27] This indicates that PEG_{6k}-AuNPs spontaneously accumulate at the interface without any salts in solutions albeit dispersed at low coverage. As shown in Fig. S1, the corresponding GISAXS pattern of unfunctionalized (bare) AuNPs without PEG does not show any features associated with the form factor. Although GISAXS patterns from aqueous solutions of pure PEG_{6k} without or with salts do not show any features different from water surface in the current Q_{xy} window (Fig. S1), PEG itself has been reported to form Gibbs monolayers at the air-water interface.[28,29,38–40] Clearly, PEG drives the functionalized PEG_{6k}-AuNPs to the gas-water interface. However, as the GISAXS pattern shows, the particles are not correlated. By contrast, in the presence of 500 mM K_2CO_3, up to 5 sharp Bragg rods become apparent, evidencing the formation of a long-range ordered crystalline layer of PEG_{6k}-AuNPs at the interface. Figure 1b shows horizontal linecut profiles along Q_{xy} direction (at Q_z = 0.020 Å^{-1}) from the GISAXS patterns in Fig. 1a. The linecut profile from PEG_{6k}-AuNPs mixed with 500 mM K_2CO_3 represents a combination of both form factor (See SAXS data from bulk solution

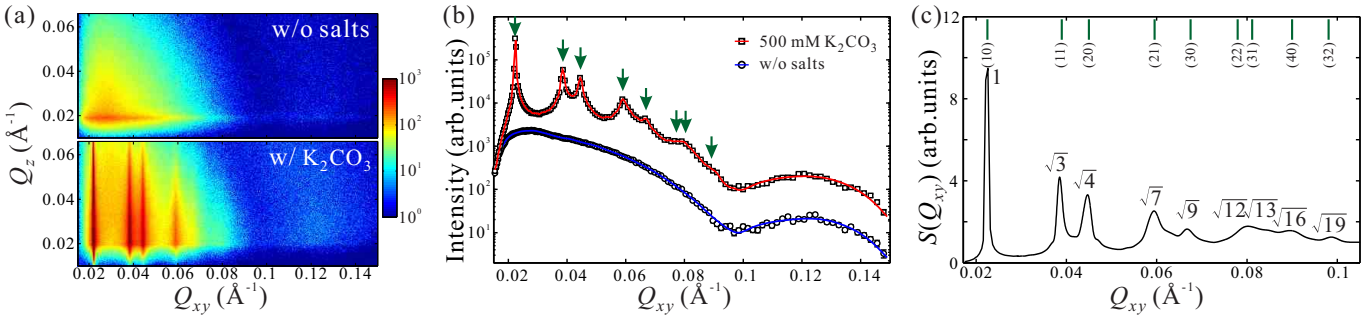

Fig. 1 K_2CO_3 induced 2D superlattices of PEG_{6k}-AuNPs at the vapor-liquid interface. (a) GISAXS patterns as functions of Q_{xy} and Q_z for aqueous solutions of 5 nM PEG_{6k}-AuNPs in the absence of salts and in the presence of 500 mM K_2CO_3. Intensities are displayed on logarithmic scales. (b) Horizontal linecut profiles along Q_{xy} direction at Q_z = 0.020 Å^{-1} integrated over Q_z range 5 $\times 10^{-3}$ Å^{-1} in the GISAXS 2D patterns for Gibbs monolayers of PEG_{6k}-AuNPs in the absence of salts (circles) and in the presence of 500 mM K_2CO_3 (squares). Solid lines are guides to the eyes. The arrows point to the calculated positions of higher orders Bragg reflections based on the the fundamental diffraction peak of a 2D hexagonal lattice. The plots are vertically shifted for clarity. (c) The extracted structure factor, $S(Q_{xy})$, profile at low Q_{xy} range (0.02–0.1Å^{-1}) for the Gibbs monolayer of PEG_{6k}-AuNPs mixed with 500 mM K_2CO_3. The peak positions ratios with respect to the fundamental diffraction peak of $1:\sqrt{3}:\sqrt{4}:\sqrt{7}:\sqrt{9}...$ reveals a hexagonal packing of nanoparticles with corresponding diffraction indices (10), (11), (20), (21), (30) and higher-order Bragg reflections.

in Fig. S2) and structure factor.[24,27] The extracted structure factor at the low Q_z range (0.02–0.1Å^{-1}) is plotted in Fig. 1c. The diffraction peak-positions ratios with respect to the fundamental peak ($Q_1 = 0.0225$ Å^{-1}) satisfy $Q_i/Q_1 \approx 1:\sqrt{3}:\sqrt{4}:\sqrt{7}:\sqrt{9}...$ (i = 1–9) revealing the formation of a long-range ordered 2D hexagonal superlattice of AuNPs with an inter-particle distance of $a_L = 4\pi/(\sqrt{3}Q_1) = 322$ Å, where the corresponding diffraction peaks are indexed as (10), (11), (20), (21), (30) and higher-order Bragg reflections. This demonstrates that K_2CO_3 plays a crucial role in promoting interfacial self-assembly and crystallization of PEG_{6k}-AuNPs. Recently, single-stranded DNA functionalized AuNPs (ssDNA-AuNPs) have been found to form a Gibbs monolayer and crystallize as hexagonal superlattices at the vapor-liquid interface.[22–24] Here, the PEG_{6k}-AuNP/K_2CO_3 exhibits much higher crystalline quality exemplified by nine Bragg reflections. Below, we describe the evolution of PEG_{6k}-AuNP superlattices systematically by regulating K_2CO_3 or PEG-AuNP concentrations.

The GISAXS patterns in Fig. 2a for aqueous solutions of 5 nM PEG_{6k}-AuNPs mixed in varying amounts of K_2CO_3 in the range of $0.05-1$ M indicate an in-plane structural transformations from uncorrelated to short-range ordering, and eventually to long-range hexagonal order at threshold concentration of about 5 mM K_2CO_3. Furthermore, the linecut profiles in Fig. 2b show that the hexagonal inter-particle distance decreases with the increase of salt concentration, as evidenced by gradual peaks-positions shift to higher Q_{xy} values. This demonstrates that K_2CO_3 is capable of tuning the 2D hexagonal superlattice at the vapor-liquid interface such that the lattice constant a_L takes values in the range $a_L = 245-388$ Å under the current tested conditions (see more details in Table 1). For concentrations $5-500$ mM K_2CO_3, the diffraction peaks are extremely sharp with a peak full-width-at half maximum (FWHM) of the (10) reflection (FWHM$_{(10)} \approx 0.0003-0.0006$ Å^{-1}) that is comparable to the instrumental resolution (≈ 0.0003 Å^{-1}), suggesting that the estimated crystalline size is on the micrometer scale, significantly larger than that found in 2D superlattices formed by ssDNA-AuNPs.[22,24] At the highest K_2CO_3 concentration (1 M) the FWHM$_{(10)} \approx 0.0019$ Å^{-1} with a 2D crystalline size on the order of 3.4 $\times 10^3$ Å, which is still superior than that found in ssDNA-AuNPs superlattices.[22,24] This trend suggests that higher K_2CO_3 concentrations, while promoting the formation of denser packing of AuNPs, induce defects in the superlattices and tend to decrease the crystalline size (Table 1).

In addition to its dependence on K_2CO_3 concentration, the self-assembly depends on the PEG_{6k}-AuNP concentration, as shown in Fig. S3 at a fixed K_2CO_3 500 mM at various concentrations of PEG_{6k}-AuNPs ($0.05-10$ nM). The GISAXS patterns as well as the corresponding linecut profiles in Fig. S3b show that short-range hexagonal order emerges at $0.25-0.5$ nM PEG_{6k}-AuNPs, and at higher concentrations long-range order of micrometer size 2D crystallines sets in with $a_L = 338 \pm 4$ Å and $a_L = 309 \pm 3$ Å at 2.5 and 10 nM, respectively (see Table 1). Qualitatively, the effect of nanoparticle concentration on monolayer density and compressibility can be understood via the Gibbs adsorption. Increasing the nanoparticle concentration in the bulk leads to an increase of nanoparticle surface density and the corresponding increase of surface pressure, originating from the entropy and inter-particle interaction, similar to the soft crystallization of ssDNA-AuNPs.[8]

AuNPs functionalized with a shorter chain PEG (MW = 800) show similar 2D superlattices under similar conditions to those used for PEG_{6k}-AuNPs discussed above. GISAXS patterns in Fig. S4 show the evolution of the self-assembly and crystallization of a fixed concentration PEG_{800}-AuNPs and varying the amount of K_2CO_3 in solution, and Fig. S5 shows the development at a fixed 500 mM K_2CO_3 for various PEG_{800}-AuNPs concentrations. Compared to PEG_{6k}-AuNPs, the diffractions peaks of PEG_{800}-AuNPs shift to larger Q_{xy} values, evidence for closer packing as expected for a shorter and smaller dynamical radius of PEG_{800}-AuNPs (See Fig. S7). We note that crystallization of PEG_{800}-AuNPs is observed only for high concentrations of K_2CO_3 and PEG-AuNPs, i.e., $a_L = 149 \pm 1$ Å at 1 M K_2CO_3 and 5 nM PEG_{800}-AuNPs, and $a_L = 158 \pm 1$ Å at 500 mM K_2CO_3 and 10 nM PEG_{800}-AuNPs.

To determine the density profile of the crystalline film across

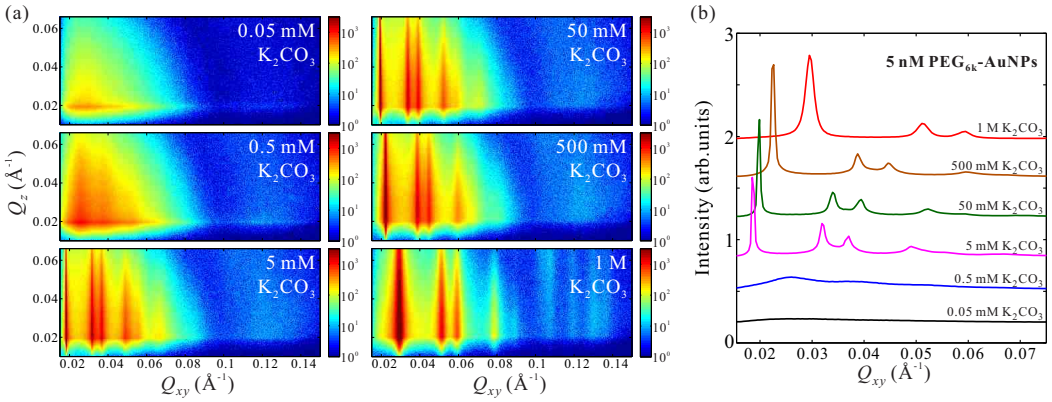

Fig. 2 In-plane structure evolution of 2D superlattices from aqueous solutions of 5 nM PEG_{6k}-AuNPs at various K_2CO_3 concentrations. (a) GISAXS patterns as functions of Q_{xy} and Q_z for aqueous solutions of 5 nM PEG_{6k}-AuNPs in the presence of 0.05 to 1 M K_2CO_3. Intensities are displayed on logarithmic scales. (b) Horizontal linecut profiles along Q_{xy} direction at Q_z = 0.020 Å^{-1} integrated over Q_z range 5 $\times 10^{-3}$ Å^{-1} at low Q_{xy} range (0.02–0.07Å^{-1}) for Gibbs monolayers of 5 nM PEG_{6k}-AuNPs at various K_2CO_3 concentrations as indicated. The plots are vertically shifted for clarity.

Table 1 Lattice parameters of 2D superlattice of PEG_{6k}-AuNPs at the vapor-liquid interface induced by K_2CO_3

[PEG_{6k}-AuNPs] (nM)	[K_2CO_3] (mM)	Q_1 (Å^{-1})	Lattice constant, a_L (Å)	FWHM (Å^{-1})	Estimated crystalline size (Å)
5	5	0.0187	388 ±4	~0.0003	2.1 $\times 10^4$
5	50	0.0198	366 ±5	~0.0004	1.5 $\times 10^4$
5	500	0.0225	322 ±3	~0.0006	1.0 $\times 10^4$
5	1000	0.0296	245 ±2	~0.0019	3.4 $\times 10^3$
2.5	500	0.0215	338 ±4	~0.0007	8.4 $\times 10^3$
5	500	0.0225	322 ±3	~0.0006	1.0 $\times 10^4$
10	500	0.0235	309 ±3	~0.0004	1.7 $\times 10^4$

the interface we employ X-ray reflectivity, which provides the electron density (ED) profile, ρ, as function of depth (along z-axis, i.e., the surface normal) by refining a model that fits the reflectivity data through the Prarratt's recursive method.[36,41,42]

Figure 3 shows X-ray reflectivity normalized to that of ideally flat water, R/R_F, for PEG_{6k}-AuNPs and PEG_{800}-AuNPs at 5 nM in the presence of different amounts of K_2CO_3 in the aqueous subphase as indicated (these are the same samples on which the GISAXS described above have been performed). The dramatic increase of the first maximum in R/R_F with the concentration of K_2CO_3, as shown in both (a) and (c) signals a huge accumulation of capped-AuNPs at the interface. Quantitative analysis of the R/R_F, based on the effective-density model[43], yields the corresponding ED profiles shown in (b) and (d) with an enhancement region over that of the solution on a $\sim$ 100 Å length scale, very close to the diameter of AuNPs (D = 88 ± 9 Å, see Fig. S2). The ED of densely packed PEG as well as water-saturated-PEG is very close to that of the water subphase, therefore yielding only a small increase in the ED of the submerged polymer tails, whereas at the air/particle interface, a $\sim$ 50 Å strata can be associated with densely-packed PEG, as depicted in Fig. 4. This practically indicates that the films that are formed at the surface consist of a mono-particle layer, and combination of the GISAXS and R/R_F results allows determination of surface coverage and conformation of the particles as discussed below. We note that the maximum R/R_F for PEG_{800}-AuNPs film are much higher than PEG_{6k}-AuNPs under otherwise identical conditions (i.e., concentrations of AuNPs and K_2CO_3). This higher surface density compared to PEG_{6k}-AuNPs is consistent with the corresponding difference in lattice parameters of the two capped-AuNPs. Based on the measured lattice parameters obtained by GISAXS, the ED of a thin slab of 2D crystalline and using a simple space filling model (See details in SI), we estimate the surface coverage of pure 2D hexagonal superlattice is nearly 100 %. The observation of limited lattice constant tunability for the shorter PEG indicates that the relatively more rigid PEG_{800}-AuNPs remain in the liquid state (short range order) over a wider range of salt concentrations compared to the softer PEG_{6k}-AuNPs.

Our main results are summarized in phase-diagrams of PEG-AuNPs versus K_2CO_3 concentrations as shown in Fig. 5 for both polymers. At low K_2CO_3 and PEG-AuNPs concentrations, the accumulated particles at the interface lack any order forming a gas-like phase. In the intermediate concentrations of K_2CO_3 and PEG-AuNPs, more PEG-AuNPs adsorb at the interface and promote formation of liquid-like state of short-range hexagonal order. At threshold concentrations of K_2CO_3 and PEG-AuNPs, a long-range order phase of 2D hexagonal superlattices is established with total surface coverage (nearly 100 %). At concentrations $\geq$ 1 M K_2CO_3 the PEG-AuNPs precipitate most likely in simple 3D structure (fcc, for instance). The phase diagram of PEG_{6k}-AuNPs shows that the lattice constant can be tuned by both K_2CO_3 and PEG-AuNP concentrations without loss of materials due to pre-

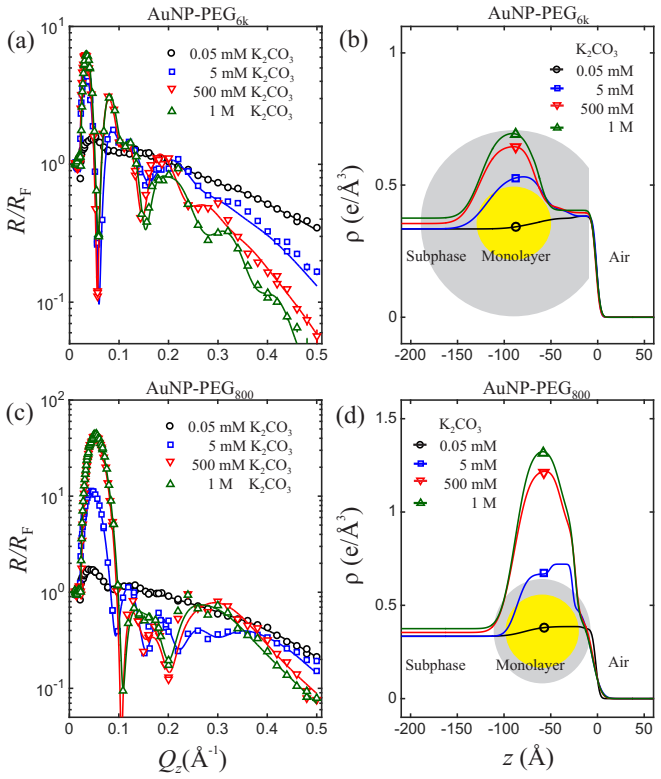

Fig. 3 Surface-normal structure evolution of 2D superlattices from aqueous solutions of PEG-AuNPs mixed with different K_2CO_3 concentrations. Representative R/R_F data for (a) PEG_{6k}-AuNPs and (c) PEG_{800}-AuNPs with same nanoparticle concentration (5 nM) at various K_2CO_3 concentrations as indicated. (b) and (d) are one of the best-fit electron density (ED) profiles that regenerate the R/R_F in (a) and (c) (solid lines), respectively.

cipitation. By contrast, in the phase diagram of PEG_{800}-AuNPs, the phase boundaries between the three 2D phases shift to high K_2CO_3 and PEG-AuNP concentrations, and thus the superlattice region without precipitation is suppressed. This indicates that the tunability in lattice constant PEG_{6k}-AuNPs is due to the compressibility of the corona from the longer chain PEG as shown schematically in Fig. 4. We argue that the tunability of the lattice constant of the PEG_{6k}-AuNP supercrystals is by virtue different from that in ssDNA-AuNP superlattices.[23,24] The ssDNA chains behave as polyelectrolytes such that the added salts screen charges of phosphate groups on the ssDNA backbones and cause the shrinkage of ssDNA chains as have been observed in X-ray scattering and dynamic lighting scattering (DLS) measurements accounting for lattice constant changes as a function of salt concentrations.[24] By contrast, while PEG-AuNPs show K_2CO_3 induced tunability of lattice parameters, the ED profiles extracted from the XRR do not show clear changes on overall monolayer thickness (including Au cores and PEG shells) along the surface-normal direction (Fig. 3), and furthermore, the DLS measurements of PEG-AuNPs dispersed in the bulk solution with and without salts do not exhibit any differences of hydrodynamic size (Fig. S7). This indicates that during formation of PEG-AuNP superlattices at the vapor-liquid interface the PEG shells bear isotropic forces along the in-plane directions conforming to the hexagonal packing. Below, we provide brief general properties of the PEG used in this study based on literature[44] and theoretical characterization of the PEG-AuNPs in terms of brush-polymer on spherical surfaces, and rationalize the accumulation and crystallization at the solution interface (more details are provided in the SI).

Based on the reported phase diagrams of PEG-salt solutions[31,32], there is a single and a two phase region, consisting of a high salt and a low salt plus PEG phases. Even in the region of the single component phase, our results show finite interfacial accumulation suggesting that there is a depletion of ions within the spherical brush, which induces an osmotic pressure gradient. Nevertheless, we find that the effect of salt (0 to 0.5 M) on the hydrodynamic radius of PEG-AuNPs is negligible (see SI). This observation can be explained by a blob size ξ that is smaller than the thermal correlation length ξ_T, thus leading to chains that are ideal and a solvent (water+salt) inside the brush that is at the θ-point.[45,46] Still, the overall surface tension of the entire brush with the poor solvent (high salt concentration) is very significant (of order $60-250k_BT$ for PEG_{6k}-AuNPs), so the PEG-AuNPs readily migrate to the interface, where such surface tension can be drastically reduced. Under this picture, the effective (hydrodynamic) spherical radius of a given PEG-AuNP (R_h) with Au-core radius R is given by[45,46]

$$\left(\frac{R_h}{R}\right)^2 = 1 + 2\frac{Nb^2\sigma^{1/2}}{R}(2w_0)^{1/4}\,, \qquad (1)$$

where N is the number of Kuhn monomers, b is the Kuhn length ($b = 7.24$ Å for PEG), σ is the grafting density (≈ 1.51 chains/nm^2), and w_0 is a dimensionless three body interaction, where we use the Flory result $w_0 = 1/6$, so that $(2w_0)^{1/4} = 0.76$.[47,48] Using the parameters derived in the SI yield $D_h = 2R_h = 35.5$ nm consistent with the measured $39.9(13)$ nm for PEG_{6k}-AuNPs whereas for PEG_{800}-AuNPs, $D_h = 15.3$ nm, significantly shorter than the measured $22.3(7)$ nm. We note that Eq. 1 is valid for an infinite chain and that PEG_{800} consists of only ≈ 9 independent (Kuhn-length) segments, suggesting a much more rigid polymer corona. Indeed the phase diagram for PEG_{800}-AuNPs shows a very narrow range of crystallinity as the corona around the particle is much less compressible than that of the longer polymer. It is interesting to note that the measured hydrodynamical radius R_h does not shrink with the increase of ionic strength, as is usually observed for polyelectrolytes-brushes or ssDNA-AuNPs,[24] but rather migrate to the interface to maintain minimal chain-contact with the poor solvent and form a densely packed hexagonal lattice - compressible for the long chain PEG and incompressible for the shorter chain. As detailed in the SI and the use of dynamic lattice theory (DLT)[49], the lattice constant at the interface (a_L), can be determined by the balance between the surface tension and the compression of the brush, leading to a simplified form that shows the dependence of the lattice constant on PEG-AuNP concentration n_s and the surface tension between PEG and the

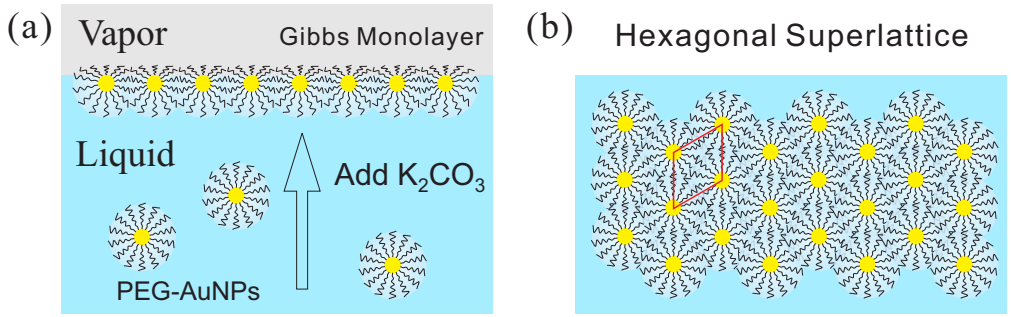

Fig. 4 A schematic of 2D self-assembly and crystallization of PEG-AuNPs at liquid-vapor interface induced by K_2CO_3 (a) side view and (b) top view.

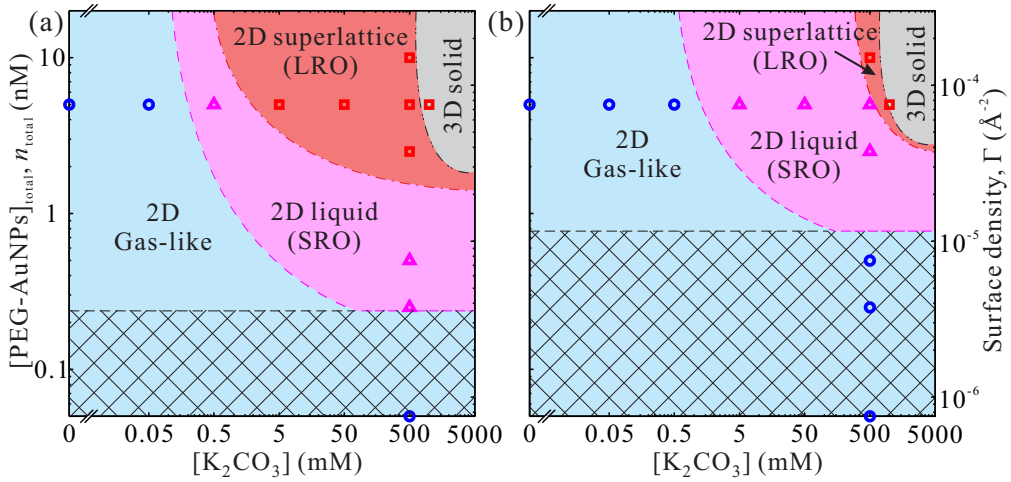

Fig. 5 Phase diagram as functions of concentrations of K_2CO_3 and total PEG-AuNPs in the system of (a) PEG_{6k}-AuNPs, (b) PEG_{800}-AuNPs. The presumptive surface density of PEG-AuNPs (number of NPs/surface area) is provided on the right axes. The symbols (circles, triangles and squares) are presented as sample conditions measured by GISAXS and XRR. The Gibbs monolayer consists of 2D gas-like (uncorrelated), 2D liquid (short range ordering, SRO) and 2D superlattice (long range ordering, LRO) phases at various conditions. 2D superlattice phase becomes unstable and form visible precipitates (3D solid) above 1 M K_2CO_3 as confirmed by SAXS. The crosshatching area below the critical surface density Γ_c indicates that the interfaces could not be fully covered by PEG-AuNPs if all the PEG-AuNPs had migrated to the interfaces. The Γ_c is calculated as $1/(R_h + \Delta R_h)^2$, where R_h and ΔR_h are the mean and spread of hydrodynamic radii of PEG-AuNPs, respectively. Note: The phase boundaries are by no means exact and they are surmised based on the limited datasets.

high salt solution γ_{AB},

$$\frac{a_L}{2} = R_h \left[1 - c_1 \left(\frac{\gamma_{AB} b^2}{k_B T} - c_2 \log(n_s/c_3) \right)^{1/3} \right] , \qquad (2)$$

where the constants c_1, c_2, c_3 can be identified in Eq. S24. Although, considerable approximations are made to derive Eq. 2, the formula illustrates the dependence of the lattice constant on surface tension and PEG-AuNP concentration n_s, in particular, the requirement that $\frac{\gamma_{AB} b^2}{k_B T} > c_2 \log(n_s/c_3)$, which sets a threshold on the lowest PEG-AuNP concentration where crystallization occurs. To apply Eq. 2 (or the more rigorous Eq. S23) a dependence of γ_{AB} on ionic strength is needed, which is expected to vary as $\frac{\gamma_{AB} b^2}{k_B T} \approx (v/b^3)^2 = (1-2\chi)^2$, where v is the excluded volume and $\chi > 1/2$ is the Flory parameter for PEG in the poor solvent high salt solution. Although attempts to determine χ [50,51] have not been very successful, see Refs.[30,31], χ is an increasing function of ionic strength. We have fitted Eq. 2 to a simple logarithmic dependence, $\frac{\gamma_{AB} b^2}{k_B T} = \tau \log(I/I_0)$, which captures qualitatively well the dependence of the lattice constant at moderate salt concentrations, is not too high, assuming solvent quality between $0.51 < \chi < 0.65$. This is consistent with the assumption that the blob size is less than the thermal correlation length. Perhaps the most important result of our analysis is that the dependence of the surface tension on ionic strength is considerably stronger than a simple logarithm at high ionic strengths, which may lead to the assembly of PEG-AuNPs via colloidal destabilization into 3D supercrystals.

4 Conclusion

Using synchrotron X-ray diffraction at small angles (GISAXS) and X-ray reflectivity (XRR) we demonstrate that functionalized complexed PEG-AuNPs in aqueous solutions can spontaneously accumulate at the vapor-solution interface by manipulating salt concentrations in the bulk (K_2CO_3, in this case). At very low salt concentrations, the XRR indicates the formation of a mono-particle layer and the GISAXS patterns show features of a form factor characteristic of individual uncorrelated spherical particles. As the salt concentration increases, short-range 2D hexagonal order develops and above a threshold concentration, the complexes exhibit highly ordered hexagonal crystallinity. Furthermore, the size of the hexagonal unit cell formed by the long chain PEG_{6k}-AuNPs can be varied appreciably by increasing salt concentration, such that the incipient lattice parameter a_L can be varied from 39 to 25 nm for 0.005 to 1 M K_2CO_3, respectively. Similar unit cell shrinkage can also be achieved by manipulating the PEG_{6k}-AuNP concentration at a moderate 0.5 M K_2CO_3. For the shorter chain PEG_{800}-AuNPs, the threshold salt concentration for crystallinity is significantly higher than that of the longer PEG_{6k} and the range of varying the unit cell size is much narrower, $a_L \sim 15 \pm 1$ nm. Our detailed analysis reveals a nearly perfect surface coverage (close to 100%) of densely packed macroscopic crystalline domains (average domain size larger than micro-meter). These results show that the surface density (i.e., unit-cell size) scales with the chain-length but more importantly they also reflect on the conformation of the corona formed by tethered PEG brushes on curved surfaces. In a salt free solution, the long chain PEG_{6k} corona is consistent with an infinitely long brush in θ-solvent. However, we find that the hydrodynamic radius of the PEG-AuNPs is practically independent of salt concentration (up to 0.5 M). Heuristically, this can be explained in terms of an effective semipermeable membrane surrounding the corona that maintains a constant salt concentration up to the θ-point. Effectively, the PEG-AuNPs reside in a low salt concentration (liquid A) that is separated at the boundaries of the corona from high concentration salt (liquid B) with an effective surface tension γ_{AB} between the two liquids. Even though the surface tension energy per polymer is low (less than $k_B T$), thus preventing the polymer from shrinking, the overall surface tension for the entire PEG-AuNP is very large (of order of $100 k_B T$ or more for the PEG_{6k}-AuNPs) and drives the self-assembly and, through optimization of the packing of PEG chains, to crystallization. The tunability of the 2D hexagonal superlattice structure can be achieved over a very wide range by manipulating salt or PEG-AuNPs concentrations and also by the choice of polymer length. Here, we also provide a method to engineer 3D crystals, since sufficiently high salt or PEG-AuNP concentrations induce the formation of 3D precipitates (see Fig. 5), which will be further explored and optimized in the future.

5 Acknowledgments

We thank Ivan Kuzmenko at beamline 9ID-B, APS, Argonne National Laboratory for technical support in liquid surface scattering measurements. We acknowledge Xiaobin Zuo at beamline 12ID-B, APS, Argonne National Laboratory for technical support in measuring bulk SAXS. H.Z. thanks Prof. Mufit Akinc (Ames Laboratory and Iowa State University) for useful discussions on the phase diagram. Research was supported by the U.S. Department of Energy (U.S. DOE), Office of Basic Energy Sciences, Division of Materials Sciences and Engineering. Ames Laboratory is operated for the U.S. DOE by Iowa State University under Contract No. DE-AC02-07CH11358. Use of the Advanced Photon Source, an Office of Science User Facility operated for the U.S. DOE Office of Science by Argonne National Laboratory, was supported by the U.S. DOE under Contract No. DE-AC02-06CH11357.

References

1 E. V. Shevchenko, D. V. Talapin, N. A. Kotov, S. O'Brien and C. B. Murray, *Nature*, 2006, **439**, 55–59.

2 Y. Zhang, F. Lu, K. G. Yager, D. van der Lelie and O. Gang, *Nat. Nanotechnol.*, 2013, **8**, 865–872.

3 K. L. Young, M. B. Ross, M. G. Blaber, M. Rycenga, M. R. Jones, C. Zhang, A. J. Senesi, B. Lee, G. C. Schatz and C. A. Mirkin, *Adv. Mater.*, 2014, **26**, 653–659.

4 D. Nykypanchuk, M. M. Maye, D. van der Lelie and O. Gang, *Nature*, 2008, **451**, 549–552.

5 S. Y. Park, A. K. R. Lytton-Jean, B. Lee, S. Weigand, G. C. Schatz and C. A. Mirkin, *Nature*, 2008, **451**, 553–556.

6 R. J. Macfarlane, B. Lee, M. R. Jones, N. Harris, G. C. Schatz and C. A. Mirkin, *Science*, 2011, **334**, 204–208.

7 W. Liu, M. Tagawa, H. L. Xin, T. Wang, H. Emamy, H. Li, K. G. Yager, F. W. Starr, A. V. Tkachenko and O. Gang, *Science*, 2016,

351, 582–586.

8 W. Cheng, M. R. Hartman, D.-M. Smilgies, R. Long, M. J. Campolongo, R. Li, K. Sekar, C.-Y. Hui and D. Luo, *Angew. Chem., Int. Ed.*, 2010, **49**, 380–384.

9 S. Narayanan, J. Wang and X.-M. Lin, *Phys. Rev. Lett.*, 2004, **93**, 135503.

10 T. P. Bigioni, X.-M. Lin, T. T. Nguyen, E. I. Corwin, T. A. Witten and H. M. Jaeger, *Nat. Mater.*, 2006, **5**, 265–270.

11 D. G. Schultz, X.-M. Lin, D. Li, J. Gebhardt, M. Meron, J. Viccaro and B. Lin, *J. Phys. Chem. B*, 2006, **110**, 24522–24529.

12 A. Tao, P. Sinsermsuksakul and P. Yang, *Nat. Nanotechnol.*, 2007, **2**, 435–440.

13 V. Aleksandrovic, D. Greshnykh, I. Randjelovic, A. Frömsdorf, A. Kornowski, S. V. Roth, C. Klinke and H. Weller, *ACS Nano*, 2008, **2**, 1123–1130.

14 P. Siffalovic, L. Chitu, E. Majkova, K. Vegso, M. Jergel, S. Luby, I. Capek, A. Satka, G. A. Maier, J. Keckes, A. Timmann and S. V. Roth, *Langmuir*, 2010, **26**, 5451–5455.

15 A. T. Heitsch, R. N. Patel, B. W. Goodfellow, D.-M. Smilgies and B. A. Korgel, *J. Phys. Chem. C*, 2010, **114**, 14427–14432.

16 C. Stefaniu, M. Chanana, D. Wang, D. V. Novikov, G. Brezesinski and H. Möhwald, *Chem. Phys. Chem.*, 2010, **11**, 3585–3588.

17 C. Stefaniu, M. Chanana, D. Wang, D. V. Novikov, G. Brezesinski and H. Möhwald, *Langmuir*, 2011, **27**, 1192–1199.

18 C. Stefaniu, M. Chanana, D. Wang, G. Brezesinski and H. Möhwald, *J. Phys. Chem. C*, 2011, **115**, 5478–5484.

19 C. Stefaniu, M. Chanana, H. Ahrens, D. Wang, G. Brezesinski and H. Möhwald, *Soft Matter*, 2011, **7**, 4267–4275.

20 M. A. Mahmoud, D. O'Neil and M. A. El-Sayed, *Chem. Mater.*, 2014, **26**, 44–58.

21 M. A. Mahmoud, *J. Phys. Chem. C*, 2015, **119**, 305–314.

22 M. J. Campolongo, S. J. Tan, D.-M. Smilgies, M. Zhao, Y. Chen, I. Xhangolli, W. Cheng and D. Luo, *ACS Nano*, 2011, **5**, 7978–7985.

23 S. J. Tan, J. S. Kahn, T. L. Derrien, M. J. Campolongo, M. Zhao, D.-M. Smilgies and D. Luo, *Angew. Chem., Int. Ed.*, 2014, **53**, 1316–1319.

24 H. Zhang, W. Wang, N. Hagen, I. Kuzmenko, M. Akinc, A. Travesset, S. Mallapragada and D. Vaknin, *Adv. Mater. Interfaces*, 2016, **3**, 1600180

25 S. Srivastava, D. Nykypanchuk, M. Fukuto and O. Gang, *ACS Nano*, 2014, **8**, 9857–9866.

26 S. Srivastava, D. Nykypanchuk, M. Fukuto, J. D. Halverson, A. V. Tkachenko, K. G. Yager and O. Gang, *J. Am. Chem. Soc.*, 2014, **136**, 8323–8332.

27 W. Wang, H. Zhang, I. Kuzmenko, S. Mallapragada and D. Vaknin, *Sci. Rep.*, 2016, **6**, 26462

28 J. Israelachvili, *Proc. Natl. Acad. Sci. U.S.A.*, 1997, **94**, 8378–8379.

29 J. Zhou, F. Ke, Y.-y. Tong, Z.-c. Li and D. Liang, *Soft Matter*, 2011, **7**, 9956–9961.

30 H. D. Willauer, J. G. Huddleston and R. D. Rogers, *Ind. Eng. Chem. Res.*, 2002, **41**, 1892–1904.

31 J. G. Huddleston, H. D. Willauer and R. D. Rogers, *J. Chem. Eng. Data*, 2003, **48**, 1230–1236.

32 H. Walter, *Partitioning In Aqueous Two-Phase System: Theory, Methods, Uses, And Applications To Biotechnology*, Elsevier Science, 2012.

33 C. H. J. Choi, J. E. Zuckerman, P. Webster and M. E. Davis, *Proc. Natl. Acad. Sci. U.S.A.*, 2011, **108**, 6656–6661.

34 X.-D. Zhang, D. Wu, X. Shen, J. Chen, Y.-M. Sun, P.-X. Liu and X.-J. Liang, *Biomaterials*, 2012, **33**, 6408–6419.

35 K. Rahme, L. Chen, R. G. Hobbs, M. A. Morris, C. O'Driscoll and J. D. Holmes, *RSC Adv.*, 2013, **3**, 6085–6094.

36 D. Vaknin, X-Ray Diffraction Techniques for Liquid Surfaces and Monomolecular Layers, In *Characterization of Materials*, John Wiley & Sons, New York, 2012, Vol.2, pp 1393-1423.

37 H. Zhang, X. Liu, S. Feng, W. Wang, K. Schmidt-Rohr, M. Akinc, M. Nilsen-Hamilton, D. Vaknin and S. Mallapragada, *Langmuir*, 2015, **31**, 2818–2825.

38 M. Winterhalter, H. Bürner, S. Marzinka, R. Benz and J. J. Kasianowicz, *Biophys. J.*, 1995, **69**, 1372–1381.

39 K. Prasitnok and M. R. Wilson, *Phys. Chem. Chem. Phys.*, 2013, **15**, 17093–17104.

40 C. Fuchs, H. Hussain, E. Amado, K. Busse and J. Kressler, *Macromol. Rapid Commun.*, 2015, **36**, 211–218.

41 J. Als-Nielsen and D. McMorrow, *Elements of Modern X-ray Physics*, John Wiley & Sons, 2011.

42 P. S. Pershan, and M. L. Schlossman, *Liquid Surface and Interfaces: Synchrotron X-ray Methods*, Cambridge University Press, 2012.

43 M. Tolan, *X-Ray Scattering from Soft-Matter Thin Films: Materials Science and Basic Research*, Springer-Verlag, 1999.

44 J. E. Mark and P. J. Flory, *J. Am. Chem. Soc.*, 1963, **87**, 1415–1423.

45 M. Daoud and J. P. Cotton, *J. Phys. France*, 1982, **43**, 531–538.

46 C. M. Wijmans and E. B. Zhulina, *Macromolecules*, 1993, **26**, 7214–7224.

47 M. Rubinstein and R. H. Colby, *Polymer Physics*, Oxford University Press, 2003.

48 K. Binder and A. Milchev, *J. Polym. Sci. B Polym. Phys.*, 2012, **50**, 1515–1555.

49 A. Travesset, *J. Chem. Phys.*, 2014, **141**, 164501.

50 T. Hino and J. M. Prausnitz, *J. Appl. Polym. Sci.*, 1998, **68**, 2007–2017.

51 P. U. Kenkare and C. K. Hall, *AIChE J.*, 1996, **42** 3508–3522.

Supporting Information
Macroscopic and Tunable Nanoparticle Superlattices

Honghu Zhang,Wenjie Wang, Surya Mallapragada, Alex Travesset, and David Vaknin
Ames Laboratory, Iowa State University, Ames,Iowa 50011, USA

Control experiments

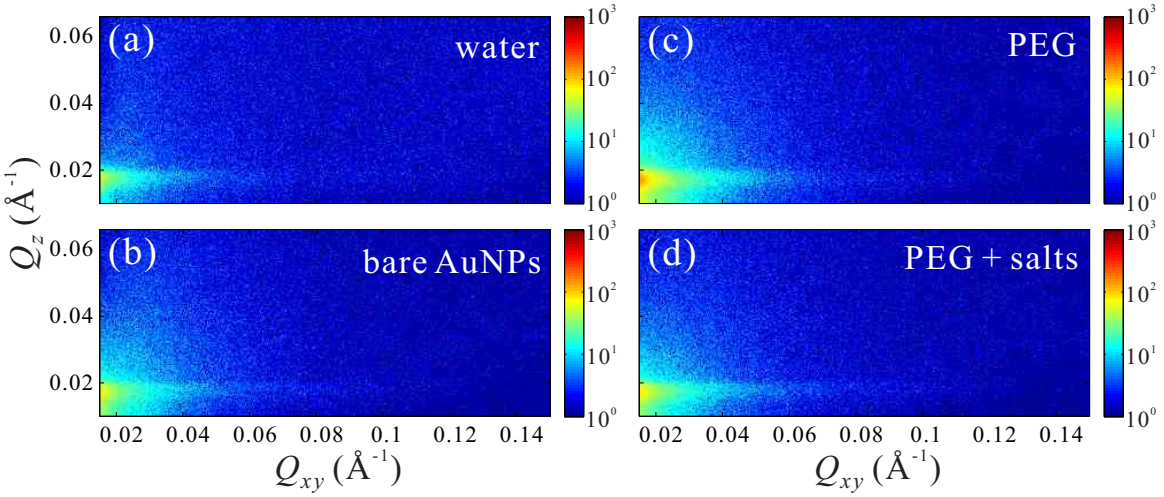

Fig. S1 GISAXS patterns as functions of Q_{xy} and Q_z for (a) pure Millipore water, (b) aqueous solution of 10 nM bare AuNPs prior to PEG functionalization, (c) aqueous solution of 10 μM PEG_{6k}-SH with no salts and (d) PEG_{6k}-SH in 500 mM K_2CO_3. Intensities are displayed on logarithmic scales

Figure S1 (a-d) shows a few GISAXS patterns from various solutions as control experiments to demonstrate the importance of functionalizing the AuNPs with PEG and the effect of salt on the formation of superlattice structures. None of the patterns indicate surface enrichment.

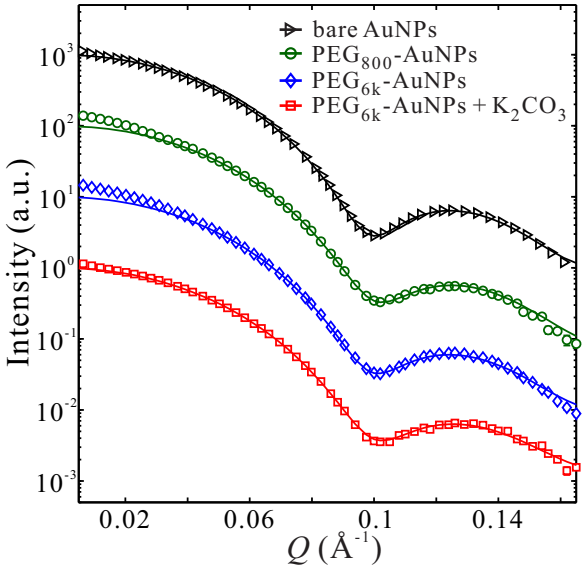

Fig. S2 SAXS intensity profiles of aqueous suspension of unfunctionalized (bare) AuNPs (black triangles), PEG_{800}-AuNPs without salts (green circles), PEG_{6k}-AuNPs without salts (blue diamonds) and PEG_{6k}-AuNPs mixed with 500 mM K_2CO_3 (red squares). The solid lines are best fits using a form factor of spherical particles with polydispersity described by a Gaussian distribution. The size distributions of nanoparticles estimated by the best fits are $D = 8.9 \pm 0.8$ nm (bare AuNPs), 8.7 ± 0.9 nm (PEG_{800}-AuNPs), 8.8 ± 0.9 nm (PEG_{6k}-AuNPs), and 8.7 ± 0.9 nm (PEG_{6k}-AuNPs with salts). These results show that the SAXS patterns are insensitive to the PEG shell around a AuNP (i.e., the corona) indicating that the electron density of the PEG corona in water solution is very close to that of pure water. The curves are vertically shifted for clarity.

Figure S2 shows SAXS measurements of PEG-AuNPs and unfunctionalized (bare) AuNPs dispersed in solution (conducted at Sector 12ID-B at the Advanced Photon Source). The analysis of the measured form factors determines the size and size-distribution of the

AuNPs. These results demonstrate that the form factor is dominated by Au cores regardless of functionalization as the corona formed by PEG around the AuNP has practically the same electron density as that of the water solution (the SAXS data in Fig. S2 are obtained after subtraction of the SAXS of the solvent). This is crucial to the analysis of the X-ray reflectivity analysis given in the main manuscript that shows the ED of the film is dominated by the AuNPs and the submerged corona is practically indistinguishable from the solution.

Superlattice dependence on PEG_{6k}-AuNPs concentrations

In the main manuscript we show the tunability of the hexagonal superlattice by varying salt concentration. Figure S3 shows the GISAXS patterns from various concentrations of PEG_{6k}-AuNPs at a fixed 0.5 M of K_2CO_3. Our theoretical model shows a dependence of the lattice constant that is logarithmic in the AuNPs concentration.

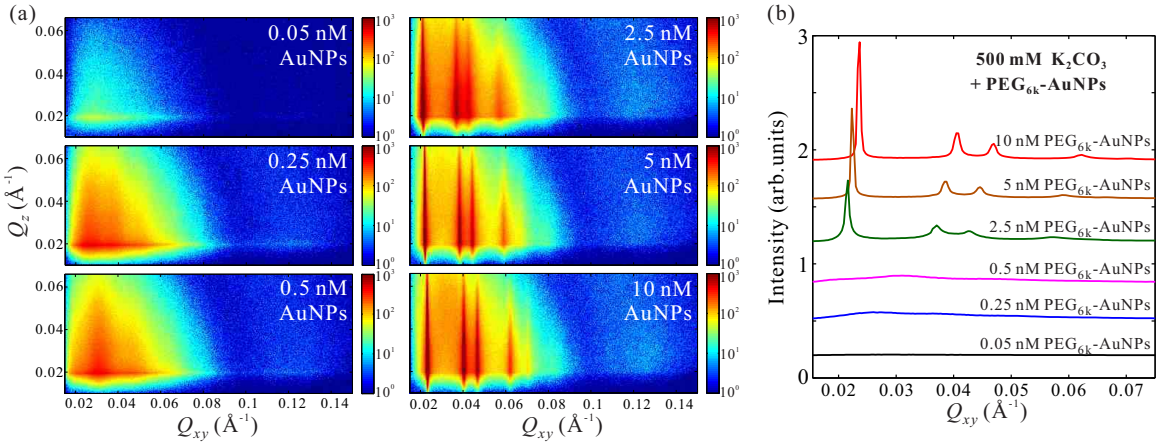

Fig. S3 (a) GISAXS patterns as functions of Q_{xy} and Q_z for aqueous solutions of PEG_{6k}-AuNPs at different nanoparticle concentrations (0.05 – 10 nM) in the presence of 0.5 M K_2CO_3. Intensities are displayed on logarithmic scales. (b) Horizontal linecut profiles along Q_{xy} direction at Q_z = 0.020 Å^{-1} integrated over Q_z range 5 $\times 10^{-3}$ Å^{-1} at low Q_{xy} range (0.02–0.07Å^{-1}) from GISAXS patterns in (a). The plots are vertically shifted for clarity.

Short chain PEG_{800}-AuNPs crystallization

In this Section, we present the evolution of the Gibbs monolayer from the gas- to liquid- to superlattice-crystallization of PEG_{800}-AuNPs both as a function of salt concentration, Fig. S4 and as a function of PEG-AuNP concentration, Fig. S5. The analysis shows that the crystallization takes place only at much higher K_2CO_3 concentrations than for PEG_{6k}-AuNPs and as expected the lattice constant scales with the length of PEG, thus the length of PEG can be used as a knob to tune the lattice constant as well.

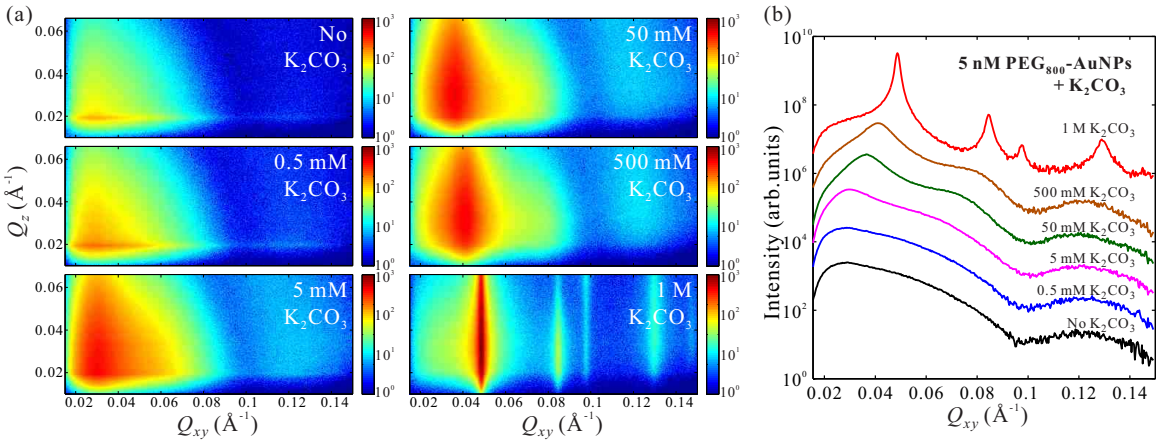

Fig. S4 (a) GISAXS patterns as functions of Q_{xy} and Q_z for aqueous solutions of 5 nM PEG_{800}-AuNPs in the absence of salts and in the presence of different concentrations of K_2CO_3 (0.5 mM – 1 M). Intensities are displayed on logarithmic scales. (b) Horizontal linecut profiles along Q_{xy} direction at Q_z = 0.020 Å^{-1} integrated over Q_z range 5 $\times 10^{-3}$ Å^{-1} at low Q_{xy} range (0.02–0.07Å^{-1}) from GISAXS patterns in (a). The plots are vertically shifted for clarity.

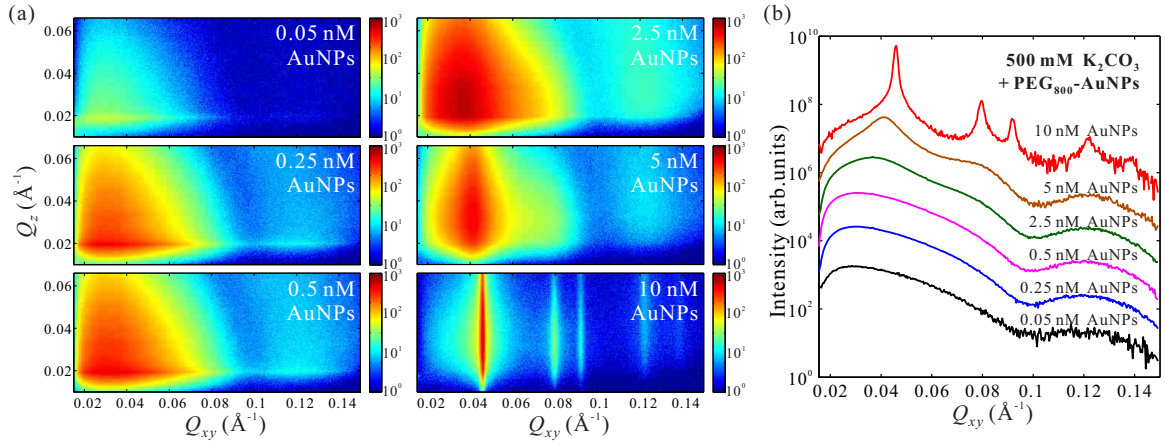

Fig. S5 (a) GISAXS patterns as functions of Q_{xy} and Q_z for aqueous solutions of PEG_{800}-AuNPs with different nanoparticle concentrations (0.05 – 10 nM) in the presence of 0.5 mM K_2CO_3. Intensities are displayed on logarithmic scales. (b) Horizontal linecut profiles along Q_{xy} direction at Q_z = 0.020 Å^{-1} integrated over Q_z range 5 $\times 10^{-3}$ Å^{-1} at low Q_{xy} range (0.02–0.07Å^{-1}) from GISAXS patterns in (a). The plots are vertically shifted for clarity.

Estimated surface coverage of crystalline PEG-AuNP superlattices

Here, we estimate the maximum in the electron density (ED) of monolayers of 2D crystalline PEG-AuNPs based on a space filling model using the known EDs of water and pure Au, and the 2D crystalline structures determined by GISAXS. We then compare our calculated maximum ED to the one obtained from the X-ray reflectivity to estimate the macroscopic surface coverage of the 2D crystalline PEG-AuNPs.

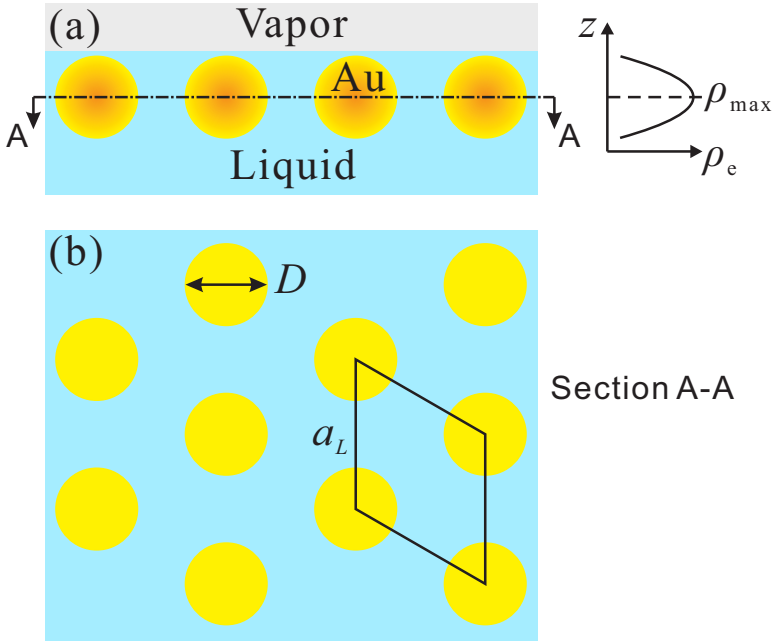

Fig. S6 A schematic of a nanoparticle monolayer at the vapor-liquid interface with corresponding ED profile along surface-normal direction, associated with the sectional view at the maximum ED position.

We assume that in the mono-particle layer of the 2D crystalline, all AuNPs are perfectly packed in the same plane, leading to a maximum ED at the plane occupied by the centers of AuNPs as illustrated in Fig. S6a. The corresponding sectional view at the maximum ED position is shown in Fig. S6b. In this maximum ED plane, the area fraction of AuNPs in the unit cell of a 2D hexagonal crystalline is $\phi = A_{\rm np}/A_{\rm 2D}$, where the area occupied by an AuNP is $A_{\rm np} = \pi D^2/4$, and the area of a 2D unit cell with a lattice constant a_L is $A_{\rm 2D} = a_L^2\sqrt{3}/2$. The ED of pure gold is $\rho_{\rm Au} = 79\rho N_A/M_{\rm Au} = 4.66$ e/Å^3, where $\rho = 19.3$ g/cm^3, $N_A = 6.02 \times 10^{23}$ mol^{-1} and $M_{\rm Au} = 196.97$ g/mol are bulk gold density, Avogadro number and atomic weight of gold, respectively. The ED of subphase area surrounding the AuNPs ($\rho_{\rm sub}$) is considered as ED of pure K_2CO_3 solution with the same concentration to the bulk (contribution of the PEG shell to the ED is the same as that of surrounding media, which is justified by our SAXS results; see Fig. S2). Assuming that K_2CO_3 solids dissolved in pure water increase the ED of aqueous solution without changing the solution volume, the ED of K_2CO_3 solution at the concentration

Table S1 Maximum electron density of 2D PEG-AuNP superlattices at the vapor-liquid interface

MW of PEG	[PEG-AuNPs] n_s (nM)	[K_2CO_3] I (M)	Lattice constant a_L (Å)	ED of K_2CO_3 solution $\rho_{K_2CO_3}$ (e/Å^3)	Estimated maximum ED ρ_{2Dmax} (e/Å^3)	Maximum ED extracted from XRR ρ_{max} (e/Å^3)	Estimated surface coverage ψ
6000	5	0.005	388 ± 4	0.3342	0.532–0.540	~0.531	≥ 96 %
6000	5	0.05	366 ± 5	0.3360	0.557–0.569	~0.557	≥ 95 %
6000	5	0.5	322 ± 3	0.3545	0.641–0.652	~0.645	≥ 98 %
6000	5	1	245 ± 2	0.3749	0.868–0.885	~0.695	≥ 63 %
6000	2.5	0.5	338 ± 4	0.3545	0.613–0.626	~0.589	≥ 87 %
6000	10	0.5	309 ± 3	0.3545	0.665–0.677	~0.617	≥ 81 %
800	5	1	149 ± 1	0.3749	1.712–1.749	~1.322	≥ 69 %
800	10	0.5	158 ± 3	0.3545	1.551–1.581	~1.783	~ 100 %

of c (in Molar) is estimated to be $\rho_{K_2CO_3} = \rho_w + 68cN_A/10^{27} = 0.334 + 0.0410c$ e/Å^3. Using the space filling model, the maximum ED of 2D crystalline structure is $\rho_{2Dmax} = \rho_{Au}\phi + \rho_{sub}(1-\phi)$. The calculated maximum ED results are summarized in Table S1 below. Overall, the estimates are close to the results measured by XRR. Applying the calculated ρ_{2Dmax} and the measured maximum ED ρ_{max} extracted from XRR, the surface coverage of 2D crystalline is $\psi = (\rho_{max} - \rho_{sub})/(\rho_{2Dmax} - \rho_{sub})$ (See Table S1). The surface coverage is nearly 100 %. We note that in this simple model the surface coverage of 2D crystalline is underestimated owing to the assumption of perfect lateral packing of AuNPs in the same plane and the negligence of surface roughness.

Hydrodynamic size of AuNPs and PEG-AuNPs in salts

Using dynamic light scattering we estimate the hydrodynamic size of bare and PEG-capped particles. Unlike polyelectrolyte-capped AuNPs (including ssDNA-AuNPs), as shown in Fig. S7, the hydrodynamic size distribution of PEG-AuNPs remains practically the same in the presence of salts. This also shows that the polymer in PEG_{800}-AuNPs is too short to behave like the theoretically infinitely long polymer brush.

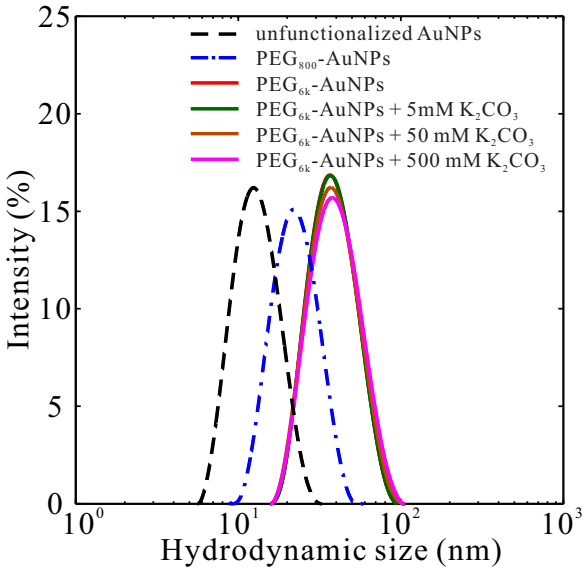

Fig. S7 Dynamic light scattering (DLS) measurements of unfunctionalized AuNPs, PEG_{800}-AuNPs and PEG_{6k}-AuNPs dispersed in the bulk solution under different conditions as indicated. The AuNPs with PEG shells clearly show larger hydrodynamic size than that of the bare Au cores (unfunctionalized AuNPs). In addition, DLS results of PEG_{6k}-AuNPs with or without K_2CO_3 indicate that the presence of K_2CO_3 in the solution (up to 0.5 M) have little effect on the hydrodynamic size of nanoparticles in the bulk.

Grafting density of PEG on AuNPs

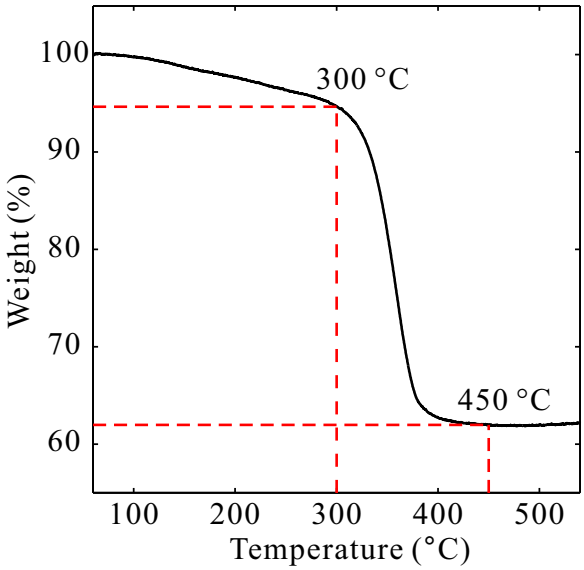

Fig. S8 Weight loss of PEG_{6k}-AuNPs as function of temperature. The weight loss between 300 °C and 450°C corresponds to the thermal degradation of the PEG.

Thermogravimetric analysis (TGA) is used to estimate the grafting density of PEG on AuNPs. The concentrated PEG-AuNPs is dried at 60 °C for 4 hours prior to TGA measurements. The TGA is carried out under a nitrogen atmosphere from 25 to 800 °C at a ramp rate of 10 °C/min. The weight loss between 300 °C and 450°C corresponds to the thermal degradation of the PEG. For instance, the weight loss of PEG_{6k}-AuNPs as function of temperature is shown in Fig. S8. The weight percentage at 300 °C and 450°C are 94.66 % and 61.96 %, respectively. Therefore, 32.70 % of weight is related to the PEG_{6k} loaded on AuNPs, and 61.96 % of weight is from pure AuNPs. The weight of each AuNP is $m_{\rm np} = \rho\pi D^3/6$, where $\rho = 19.3$ g/cm^3 is bulk gold density, $D = 8.8 \pm 0.9$ nm is the diameter of the AuNP. The molecular weight of PEG_{6k} is $m_{\rm PEG} = 6000$. Thus, the number of PEG_{6k} per AuNP is $n = (32.70 m_{\rm np})/61.96 m_{\rm PEG} = 367$. The grafting density is $\sigma = n/(\pi D^2) = 1.51$ chains/nm^2.

Theoretical Model

Physical parameters of PEG

There is a considerable range of values for the Kuhn length, Flory characteristic ratio C_n and Kuhn monomer mass M_0 in the literature. The values used here are calculated from Mark and Flory[44], who report the values for PEG (also called PEO) in salt at the θ-point, the exact conditions analyzed in this paper, as

$$\langle r^2\rangle/ml^2 = C_\infty = 4.1(0.4), \tag{S1}$$

where $\langle r^2\rangle$ is the mean square unperturbed end-to-end distance for a real chain, $l^2 = (2l_{co}^2 + l_{cc}^2)/3.0$ and $l_{co} = 1.43$ Å, $l_{cc} = 1.53$ Å are the O – C and C – C bond lengths, and $m = 3N_r$ is the number of bonds and N_r is the number of C – C – O groups in the polymer. The maximum extension of a PEO chain is therefore

$$R_{max} = (2l_{co} + l_{cc})\cos(\theta/2)N_r = 3.64N_r \ \ (\text{Å}) \ , \tag{S2}$$

where $\theta = 68^\circ$ is the bond angle, which is the same for all three atoms in the monomer. The Kuhn length is[47]

$$b = \frac{C_\infty l^2 m}{R_{max}} = 7.24 \ (\text{Å}) \tag{S3}$$

and the equivalent number of monomers of a Gaussian chain is

$$N = \frac{R_{max}^2}{C_\infty m l^2} = 0.503 N_r. \tag{S4}$$

Using that the molecular weight of a PEO monomer is $M_1 = 2M_C + M_O + 4M_H = 44.052$, it is

$$M_0 = M_1/0.503 = 87.6. \tag{S5}$$

Thus for the two PEO used in this paper, the number of independent Kuhn monomers is

$$N_{6k} = 6000/87.6 = 68.5 \ (N_r = 136) \tag{S6}$$

$$N_{800} = 800/87.6 = 9.13 \ (N_r = 18) \ . \tag{S7}$$

For the PEG_{800}, the approximation $C_n \approx C_\infty$ is certainly questionable, and explains the larger hydrodynamic radius than the theoretical estimate.

PEG-AuNPs in solution

As described in Refs.[30,31] the three component system water-salt-PEG typically separates into two phases, an all PEG solvated by liquid A and liquid B. Liquid A consists of water and a relatively low salt concentration (a few percent weight or less), and liquid B with a higher salt concentration of ten percent or more. Early efforts to predict the phase diagram of this three component system showed a limited success[50,51] as it was noted that there is a specific salt-PEG interaction, presumably through the ether oxygens and the salt cations. Therefore, we consider a model where the salt is implicit, based on the following assumptions:

- Liquid A is a θ-solvent for PEG.
- Liquid B is a poor solvent for PEG.
- When equilibrium is established, an interface between liquid A and liquid B is formed with surface tension γ_{AB}.

The first assumption is justified as liquid A is the phase boundary for PEG. The second assumption follows from the fact that no PEG is found in liquid Refs.[30,31].

We consider a PEG-AuNP as consisting of n flexible chains with N monomers covalently grafted at the surface of the nanoparticle core, whose radius is R. The grafting density is thus $\sigma = n/4\pi R^2$. We first treat PEG-AuNPs in solution and then its crystallization at the interface.

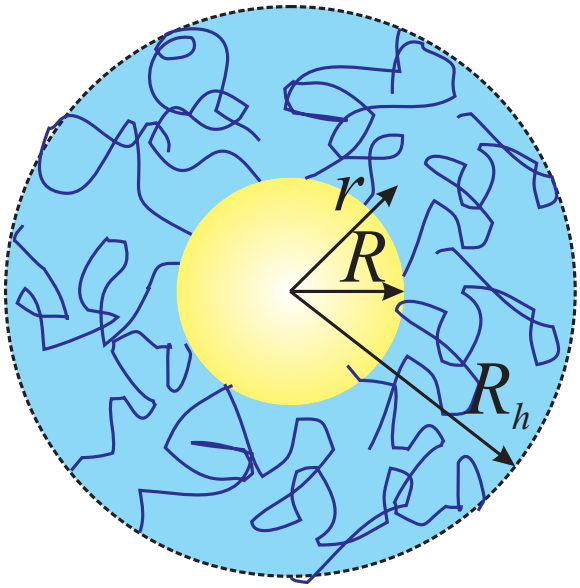

Fig. S9 Depiction of PEG-AuNP brush, and the parameters used.

Following Ref.[46], we consider PEG as gaussian chains with three-body interactions at the θ-point (first assumption). The monomer density at a distance r from the center is given (for $r > R$)

$$\phi(r) = \frac{R}{r}(\sigma b^2)^{1/2}(2w_0)^{-1/4} \ , \tag{S8}$$

where b is the Kuhn length, σ is the grafting density and w_0 is the dimensionless three-body interaction. The spherical radii R_h is obtained by imposing that the integral of the above density is equal to the total number of monomers $= Nnb^3$, leading

$$\left(\frac{R_h}{R}\right)^2 = 1 + 2\frac{N}{R/b}(\sigma b^2)^{1/2}(2w_0)^{1/4} \ . \tag{S9}$$

For future reference, we will also need the free energy for the spherical brush at the θ point. It is given as

$$\frac{f_r}{k_BT} = 4\pi\left(\frac{R}{b}\right)^3 (\sigma b^2)^{3/2}(2w_0)^{1/4}\log(1+2\frac{N}{R/b}(\sigma b^2)^{1/2}(2w_0)^{1/4}). \tag{S10}$$

To this free energy, there is an additional term that arises from the surface tension between polymer/liquid A and liquid B. We will assume that liquid B is a slightly poor solvent for PEG. This latter condition is defined by $\xi(r=R_h) < \xi_T$, where $\xi(r) = r/R\sqrt{\sigma}$ and $\xi_T = b/(2\chi-1)$ is the thermal correlation length[47], and $\chi > 1/2$ parameterizes the quality of solvent B to PEG. In the opposite limit $\xi(r=R_h) > \xi_T$, which is not discussed here, PEG would collapse into globules, and the size of the PEG-AuNPs is not described by Eq. S8. The surface tension free energy is given by

$$f_s = \gamma_{AB} 4\pi R_h^2 \, . \tag{S11}$$

Based on general arguments, we expect $\gamma_{AB} \approx k_BT(2\chi-1)^2/b^2$.

Finally, because the PEG-AuNPs are in solution, there is the ideal term

$$F_t = N_s k_BT(\log(n_s v_0) - 1) \, , \tag{S12}$$

where N_s is the number of PEG-AuNPs in solution and $n_s = N_s/V$ its number density. The chemical potential of the bulk PEG-AuNPs is given by

$$\mu_B = \frac{\partial F}{\partial N_s} = f_r + f_s + k_BT\log(n_s v_0). \tag{S13}$$

PEG-AuNPs at the interface

At the interface, the free energy of the PEG-AuNPs is modified in three ways: the brushes are compressed, the surface area of contact with solvent B is much reduced, and finally, there is a reduction of translational entropy.

The stretching energy of two compressed brushes has been authoritative reviewed in Ref.[48]. Unfortunately, no simple expression is available for the experimental conditions, and a full calculation is beyond the scope of this paper. Therefore, we opt for a more heuristic derivation, based on the modified Derjaguin approximation for the excess free energy

$$F_e(z) = 2\pi R^2(R+z)\int_z^{H_0} \frac{f(H)-f(H_0)}{(R+H)^2}dH \equiv 2\pi R^2(R+z)\int_z^{H_0}\frac{\Delta f(H)}{(R+H)^2}dH \, . \tag{S14}$$

Here, $2(R+z)$ is the center-to-center distance of the two brushes and $H_0 = R_h - R$ is the uncompressed brush height. The quantity $f(H)$ is the free energy per unit area of a uniformly compressed spherical brush at a radius $H < H_0$. It is given as

$$\Delta f(y) = \frac{R}{b}(\sigma b^2)^{3/2}(2w_0)^{1/4}\frac{1}{b^2}G(y) \tag{S15}$$

where $y = (R+z)/R_h$. Note that the function $G(x)$ satisfies that $G'(1) = 0$, $G''(1) \approx 32.6 > 0$, and the latter condition is the statement that the uncompressed brush is a minimum of the free energy. Detailed derivations for these results will be published elsewhere. The actual potential between two PEG-AuNPs is then given as

$$F_e(z) = 2\pi\left(\frac{R}{b}\right)^3 (\sigma b^2)^{3/2}(2w_0)^{1/4} y H(y) \, , \tag{S16}$$

where $H(y) = \int_y^1 \frac{dw}{w^2}G(w)$, and $G(y)$ has been defined in the previous equation. Note that $H(1) = H'(1) = H''(1) = 0$. For small compressions, $1-y << 1$, the above expression reduces to

$$F_e(z) = 2\pi\left(\frac{R}{b}\right)^3 (\sigma b^2)^{3/2}(2w_0)^{1/4}\frac{G''(1)}{6}(1-y)^3 \, . \tag{S17}$$

It should be noted, however, that the exact formula shows that the approximation Eq. S17 has a small range of applicability as the resulting potential quickly picks up significant non-harmonic contributions for $y \lesssim 0.85$.

We assume that the surface in contact with solvent B is the area of the plane occupied by the PEG-AuNPs at the interface. The free energy of a single nanoparticle is given as

$$F_s(z) = \gamma_{AB} 2\sqrt{3}(R+z)^2 \, . \tag{S18}$$

Finally, the entropic term is given, within dynamic lattice theory (DLT)[49].

$$F_d(z) = k_BT(g(R_h) + \log(v_0)) \, , \tag{S19}$$

where $g(z) = \frac{1}{2N_i}\log\left[\det(\frac{D_{ij}}{2\pi k_BT})\right]$, where N_i is the number of particles at the interface and D_{ij} is the dynamical matrix. Although it is possible to calculate the above determinant exactly for an hexagonal two dimensional lattice, the formula is excessively complex. We

therefore make the free volume approximation

$$F_d(z) = k_B T \log(v_0/(4\pi y^2 R_h^3/3)) \ . \tag{S20}$$

The chemical potential of the PEG-Au at the interface is given by

$$\mu_I = F_s(z) + qF_e(z) + F_r + k_B T \log(v_0/(4\pi y^2 R_h^3/3)) \ . \tag{S21}$$

Equilibrium condition

The condition of equilibrium between bulk and interface leads to the equation

$$\mu_I = \mu_B \ , \tag{S22}$$

or, in explicit form:

$$\begin{aligned}(4\pi - 2\sqrt{3})\frac{\gamma_{AB}}{k_B T} R_h^2 + \log(n_s 4\pi R_h^3/3) \quad &= \quad -2\sqrt{3}\frac{\gamma_{AB}}{k_B T} R_h^2 (1-y^2) + \\ &+ \quad 2\pi \left(\frac{R}{b}\right)^3 (\sigma b^2)^{3/2} (2w_0)^{1/4} y H(y) - \log(y^2) \ ,\end{aligned} \tag{S23}$$

which determines y, and from it, the lattice constant a_L from $y = \frac{2R_h - a_L}{2R_h}$, as a function of the physical parameters. The above equations illustrate a physical mechanism where the dramatic reduction in surface tension that occurs when particles reach the interface entirely drives the crystallization process.

For the purposes of illustrating the physical mechanism, one can assume that the reduction of surface tension is opposed by the stretching or compression energy, and that the small compression limit Eq. S17 can be applied. With these approximations, it follows:

$$(1 - \frac{a_L}{2R_h})^3 = (4 - \frac{2\sqrt{3}}{\pi})\frac{1}{\sigma b^2}\left(\frac{b}{R}\right)^2 \frac{6N}{qG''(1)}\left(\frac{\gamma_{AB} b^2}{k_B T} + \frac{b/R \log(n_s v_l)}{(8\pi - 4\sqrt{3})N(\sigma b^2)^{1/2}(2w_0)^{1/4}}\right) \ , \tag{S24}$$

where $v_l = \frac{4\pi}{3} R_h^3$.

Quality of the solvent

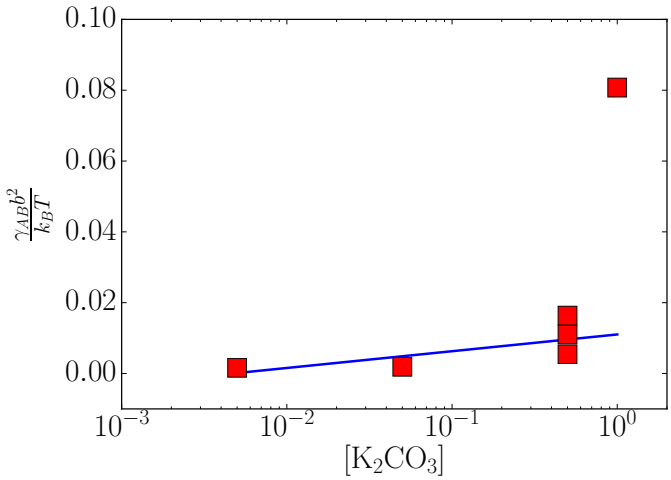

Fig. S10 Fit of the solvent quality as described below. The results are for PEG_{6k}-AuNPs. Clearly, the last point, corresponding to 1 M K_2CO_3 concentration, is not consistent with a simple logarithmic dependence

From the reported values of $\frac{2R_h - a_L}{2R_h}$ (Table S1), and the assumption that the solvent quality parameter is described by the two parameter formula

$$\gamma_{AB} b^2/k_B T = \tau log(I/I_0) \tag{S25}$$

a fit is performed, with $I_0 = 0.0046$ M and $\tau = 0.0021$. Here I is the K_2CO_3 concentration, $[K_2CO_3]$. Although the quality of the fit is adequate up to about 0.5 M, it illustrates that the data is consistent with a moderately poor solvent, not far from ideal. The point at the higher salt concentration illustrates that the surface tension grows more rapidly than the logarithmic fit Eq. S25 at high ionic strengths consistent with the onset of precipitates into 3D solids.